7

A GEOMETRIC SOLUTION FOR MULTI-PASS OVERLAYS

7.1 INTRODUCTION

In the previous chapter it was seen that, by making an empirical correction for geometric effects, significant improvements could be made to the k-ε model. It may therefore be possible to achieve further improvements by developing a model that reconstructs the geometry of an overlay.

A new model is developed here. It is based on the assumption that both the bead profile and the fusion line can be modelled by parabolic functions. A parabola is a sensible choice as it has already been found to give accurate representations of single-bead profiles at moderate-to-high travel speeds (see section 3.5). Figure 2.3 (page 19) also showed that the profile of the fusion line, as calculated for a distributed source of heat in the absence of weld pool convection, is approximately parabolic. Another advantage of the parabolic function is that it is mathematically convenient. There are only two independent coefficients to be determined, and the integration of a parabolic function is straightforward.

7.2 THE STEADY-STATE BEAD PROFILE

The overlays and single beads that were deposited for the k-ε model (see section 6.6) were closely examined. An interesting observation was made in that, when depositing

each multi-pass overlay, the bead width did not change significantly from that of the matching single-bead deposit. The bead width in each overlay was measured on a straight line from the toe of the last bead to the point on the previous bead surface where melting commenced (see Figure 7.1). The beads were generally much wider than they were high and, in each overlay, the difference between the measured bead width and the projected bead width was found to be small. (The projected bead width is the width of a bead in the overlay projected down on to the plane of the substrate surface.) In order to simplify the analysis it will be assumed that, when depositing a multi-pass overlay, the projected bead width remains constant and equal to the single-bead width.

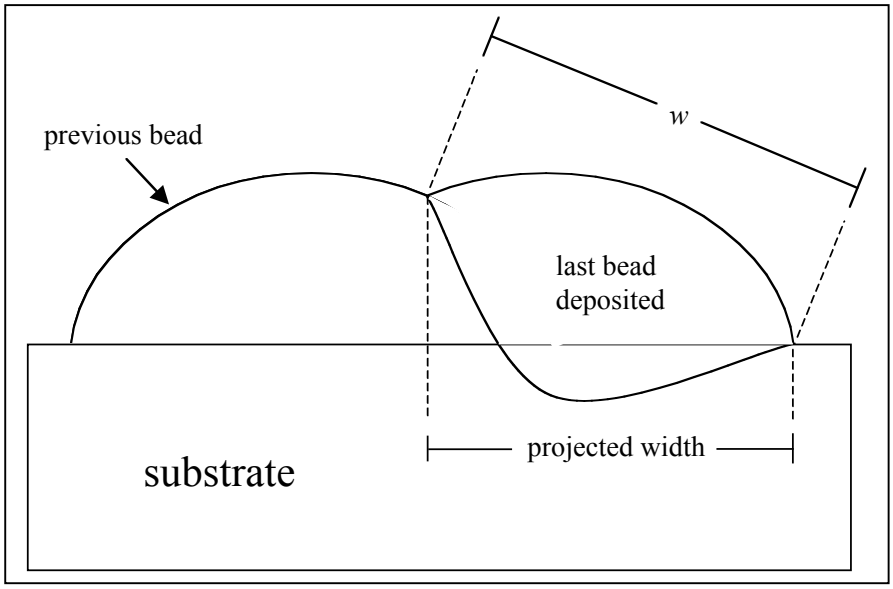

Figure 7.1: - The measurement of the true bead width, *w*, and the projected bead width for a bead in a multi-pass overlay.

Two constraints are needed to define a parabolic function. One has been provided by assuming that the projected bead width remains unchanged. The other constraint is provided by the principle of conservation of mass. Each time a bead is deposited the

correct area, A_d, must be added to the cross-sectional area of the overlay. Figure 7.2 is a schematic representation of the basis for the analysis.

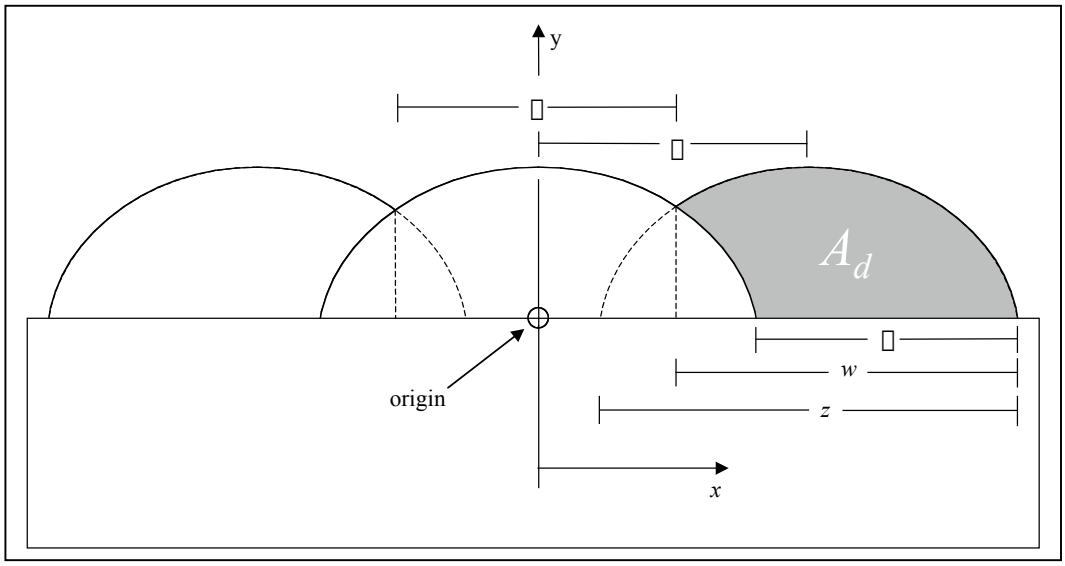

Figure 7.2: - Coordinate system for bead profile analysis. Note that the projected bead width is assumed to be equal to the single-bead width, *w*.

By observing the symmetry, the effective width of each parabola, *z*, can be seen to be given by:

$$z = \square + 2(w - \square)$$
$$\therefore \quad z = 2w - \square \qquad \cdots\cdots \quad (7.1)$$

The central parabola in Figure 7.2 will be a function of the form:

$$y(x) = H_p - a_1 x^2 \qquad \cdots\cdots \quad (7.2)$$

where H_p is the peak height of the parabola and a_1 is a constant coefficient.

It is known that:

$$y\left(\frac{z}{2}\right) = 0$$

$$\therefore \quad y\left(w \cdot \frac{\theta}{2}\right) = 0 \qquad from\ equation\ 7.1$$

$$\therefore \quad H_p - a_1\left(w \cdot \frac{\theta}{2}\right)^2 = 0$$

Rearranging gives:

$$a_1 = \frac{4H_p}{(2w \cdot \theta)^2} \qquad \cdots\cdots\cdots (7.3)$$

Substituting equation 7.3 into 7.2 gives:

$$y(x) = H_p - \frac{4H_p}{(2w \cdot \theta)^2} x^2 \qquad \cdots\cdots\cdots (7.4)$$

The projected bead width constraint has now been satisfied. All that remains is to satisfy conservation of mass. If the symmetries in Figure 7.2 are closely examined it can be seen that the shaded area represented by A_d is mathematically equivalent to the following:

$$A_d = \int_{-\frac{\theta}{2}}^{\frac{\theta}{2}} H_p - \frac{4H_p}{(2w \cdot \theta)^2} x^2 . dx$$

…… and once again by symmetry:

$$A_d = 2\int_{0}^{\frac{\theta}{2}} H_p - \frac{4H_p}{(2w \cdot \theta)^2} x^2 . dx$$

Now, the cross-sectional area of deposited material will be the same as that for a matching single bead. Thus, A_d can be replaced according to equation 6.17 (page 129) to give:

$$\frac{W}{\rho S} = 2\int_0^{\frac{w}{2}} H_p - \frac{4H_p}{(2w-\theta)^2}x^2 .dx \quad \cdots\cdots\cdots (7.5)$$

where W is the deposition rate, ρ is the density of an all-weld-metal deposit and S is the travel speed. Equation 7.5 can be solved to obtain the peak height of a parabola, H_p, explicitly:

$$H_p = \left[\frac{W}{\rho S}\right]\left[\frac{12w^2 - 12\theta w + 3\theta^2}{12\theta w^2 - 12\theta^2 w + 2\theta^3}\right] \quad \cdots\cdots\cdots (7.6)$$

Substituting equation 7.6 into equation 7.4 gives the expression for the steady-state bead profile:

$$y(x) = \left[\frac{W}{\rho S}\right]\left[\frac{12w^2 - 12\theta w + 3\theta^2}{12\theta w^2 - 12\theta^2 w + 2\theta^3}\right]\left[1 - \frac{4x^2}{(2w-\theta)^2}\right] \quad \cdots\cdots\cdots (7.7)$$

The wire feed rate (*i.e.* deposition rate), travel speed and step-over are generally known and recorded on the welding procedure sheet with other welding parameters. The density of an all-weld-metal deposit is a material property. The bead width, w, is obtainable from either direct measurement or knowledge of the welding parameters and equation 3.4 (page 44).

7.3 PEAK-TO-VALLEY RIPPLE

The peak-to-valley ripple is a parameter of great interest to the hardfacing industry. It refers to the variation in the height of an overlay from the peak of a bead to the adjacent trough. It is a measure of the smoothness of an overlay and is believed to affect the wear performance in certain applications (Wittke, 1990).

An estimate for the peak-to-valley ripple, R, is readily obtainable from equation 7.7 by using the following approach:

$$R = peak\ height - trough\ height$$

$$R = y(0) - y\left(\frac{\delta}{2}\right)$$

$$R = \frac{W}{\delta S}\left[\frac{12w^2 - 12\delta w + 3\delta^2}{12\delta w^2 - 12\delta^2 w + 2\delta^3}\right]\left[\frac{\delta^2}{(2w-\delta)^2}\right] \quad \cdots\cdots\cdots (7.8)$$

This expression for peak-to-valley ripple can be used as a check on equation 7.7. For the equation to be correct it must predict the correct ripple at each end-point, *i.e.* at 0% and 100% overlap. Zero overlap corresponds to the case where the step-over, δ, is equal to the bead width, w. In this case there will be a series of single beads side-by-side and the ripple will be equal to the single-bead height. Substituting $\delta = w$ into equation 7.8 reveals that:

$$R = \frac{3}{2}\frac{W}{\delta S w} \quad at\ 0\%\ overlap$$

This result is in agreement with equation 3.11 (page 55) and the predicted single-bead height.

Although 100% overlap is not possible in reality, the ripple must converge to zero as the step-over approaches zero. If equation 7.8 is examined it can be seen that the ripple is undefined when $\delta = 0$. This is reassuring as it is physically impossible to deposit a single-layer overlay when $\delta = 0$. In order to check the limiting value of the ripple as δ approaches zero, it is convenient to combine the two terms in δ in equation 7.8 as follows:

$$R = \left(\frac{W}{\delta S}\right)\left(\frac{12\delta^2 w^2 - 12\delta^3 w + 3\delta^4}{48\delta w^4 - 96\delta^2 w^3 + 68\delta^3 w^2 - 20\delta^4 w + 2\delta^5}\right)$$

As δ approaches zero the lower order terms in δ survive. The lowest order term in δ is a term in the denominator, δ to the power of unity. This term will dominate as δ approaches zero and consequently the quotient will converge to zero rather than diverge. This limit can be verified by applying l'Hôpital's rule for limiting values of quotients in which the numerator and denominator converge to zero simultaneously.

Equations 7.7 and 7.8 have the correct end-point values and will provide a model for the steady-state bead profile in a multi-pass overlay. Mathematically, bead overlap may assume a value between zero and 100%. In practice, however, overlaps between 40 and 60% are recommended (Gorman, 1997). Overlaps below 40% may result in a high peak-to-valley ripple, whereas overlaps above 60% may reduce penetration to a degree where there is a risk of lack of fusion.

7.4 THE FUSION LINE

Having obtained the profile of the previous bead, the next step is to determine the fusion line. The fusion line can also be modelled by a parabolic function. The two parameters that define the parabola are the width and the depth. The width is defined by the limits of melting (see Figure 7.3). Melting associated with the last bead must commence on the surface of the previous bead, at the trough between the last bead and the previous bead. Melting will cease at the toe of the last bead. It must be noted that melting will not proceed at 90^o to the x-axis; it will proceed in a direction that is perpendicular to the straight line between the limits of melting. Consequently, an $x\_$-$y\_$ coordinate system

was defined in order to describe the melting parabola. Melting will proceed at 90^o to the $x\_$ axis in Figure 7.3.

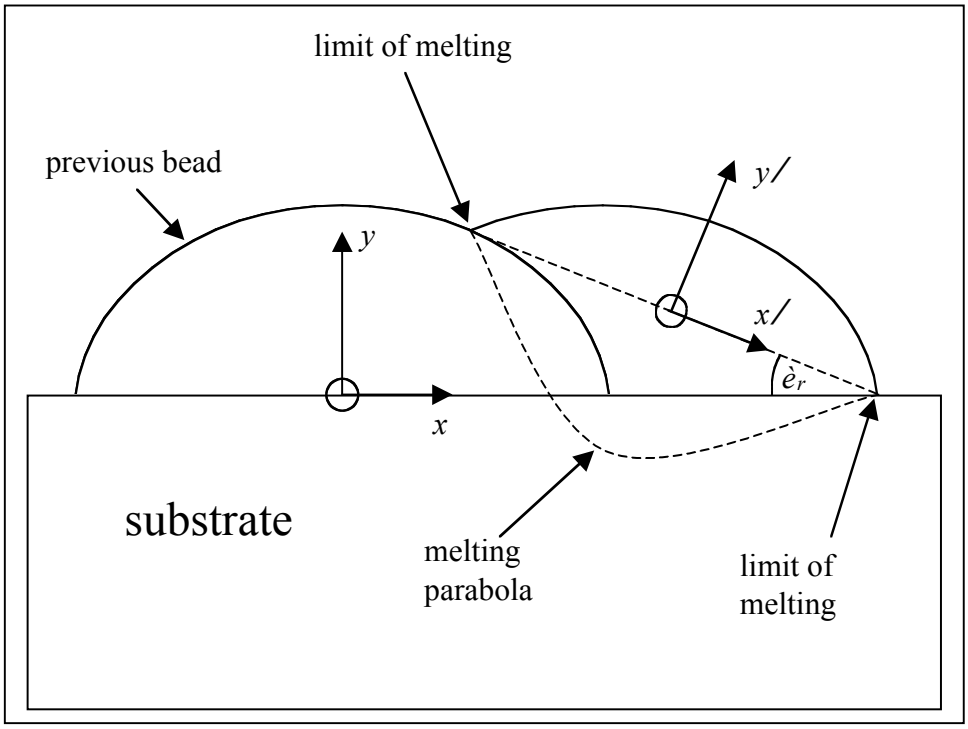

Figure 7.3: - The limits of melting and the coordinate system for the melting parabola. The coordinate system for the melting parabola is denoted $x\_$-$y\_$ in the diagram and is rotated by an angle ϕ relative to the x-y coordinate system.

The other constraint on the melting parabola is the requirement that the correct amount of material is melted. This information is obtained from the equivalent single-bead dilution. Thus a parabolic approximation to the fusion line is available. The melting parabola, however, is difficult to solve explicitly, largely due to its axis being rotated relative to the x-y coordinate system. Consequently, a spreadsheet program was developed to solve for the steady-state fusion line numerically.

7.4.1 A Spreadsheet Solution

The spreadsheet program requires the user to enter the following input data:

i. Wire feed rate (*i.e.* deposition rate, W).

ii. Travel Speed, S.

iii. Step-over, $\square$.

iv. Bead width, w.

v. Single-bead dilution, D_{sb}.

Values for the first three inputs are generally set by the operator and recorded on the welding procedure sheet. Values for the single-bead dilution and width can be predicted using equations 2.2 (page 10) and 3.4 (page 44) respectively. Alternatively, they can be measured directly by depositing a single bead-on-plate.

The bead profile and fusion line are generated in the following steps:

(a) An x-y Cartesian coordinate system is established as defined in Figure 7.2.

(b) The steady-state parabola for the bead profile is generated at discrete points (three times to represent three adjacent beads) using equation 7.7 and data inputs (i) to (iv). Each parabola is offset from its nearest neighbour by one step-over, $\square$. The all-weld-metal density, $\square$, was assumed to be 7500 kg/m^3 for high-chromium white irons. (The all-weld-metal density is a function of the volume fraction of carbides in the all-weld metal deposit. This value was obtained by assuming a total carbide volume fraction of 50% in the all-weld-metal deposit and referring to the density data of Maratray and Usseglio-Nanot (1970)).

(c) The width of the melting parabola, w^* (see Figure 7.4), is calculated using Pythagoras' theorem:

$$w^* = \sqrt{w^2 + \left(y\left(\frac{w}{2}\right)\right)^2}$$

The function $y(x)$ is given by equation 7.7.

(d) The area of substrate that is melted in a matching single-bead deposit is calculated using equation 6.18 (page 130).

(e) The melting area correction, as defined in Figure 7.5, is determined by numerical integration.

(f) The melting area correction is added to the area of substrate that is melted in a matching single-bead deposit to give the area of the melting parabola and hence the melting depth.

(g) The melting parabola is generated at discrete points in its own $x\_$-$y\_$ coordinate system.

(h) The desired angle of rotation, θ_r (see Figure 7.3), is calculated from the Pythagorean triangle described in step (c).

(i) The melting parabola is rotated, translated and plotted for each of the three bead profiles generated in step (b) to complete an image of the overlay. The rotation is achieved by performing a matrix operation on each of the discrete points generated for the melting parabola. The coordinates of a point (x', y') in the x'-y' coordinate system are converted to a point (x, y) in the x-y coordinate system by the following transformtion (Anton and Rorres, 1987):

$$\begin{bmatrix} x \\ y \end{bmatrix} = \begin{bmatrix} \cos\theta_r & \sin\theta_r \\ -\sin\theta_r & \cos\theta_r \end{bmatrix} \begin{bmatrix} x' \\ y' \end{bmatrix}$$

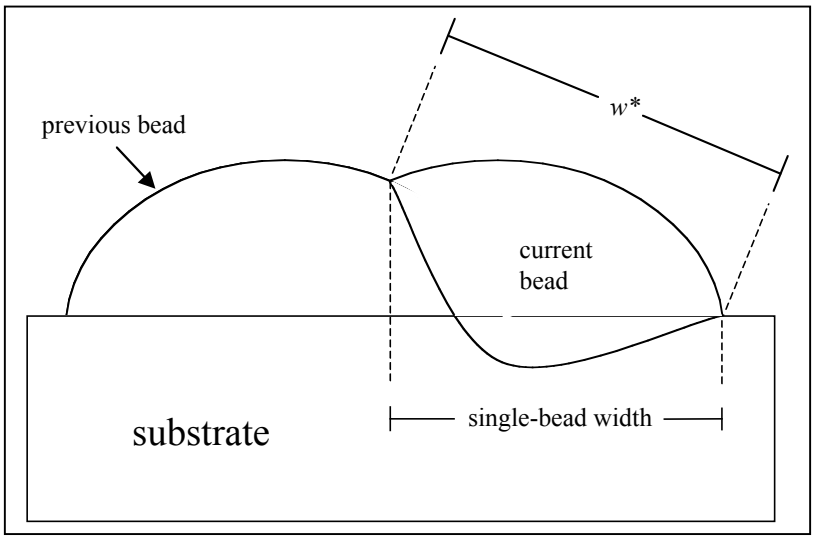

Figure 7.4: - The straight line distance between the limits of melting, *w**, is shown in the diagram. The geometric model assumes that the projected bead width is equal to the single-bead width. The width of the melting parabola, *w**, is then calculated using Pythagoras' theorem.

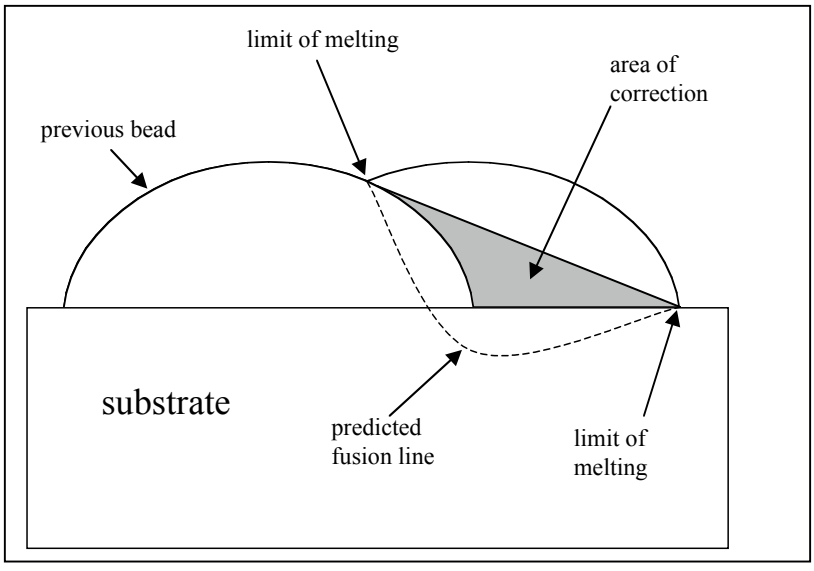

Figure 7.5: - Schematic representation of the melting area correction.

Two examples of the output from the spreadsheet program and hence the geometric model are given in Figures 7.6 and 7.7. The first welding condition corresponds to sample overlay "E" described in section 6.6 and the second to overlay "H". The deposition conditions are summarised in Table 6.2 (page 121) and details of the geometry of each sample are given in Table 6.3 (page 122).

7.5 COMPARISON WITH EXPERIMENTS

The output data from the geometric model were compared with the results of experiments "A" to "H" (see section 6.6). Once again, the test of accuracy was to determine the ability of the model to predict the average penetration of the overlay under steady-state conditions. In addition, the peak-to-valley ripples were measured for each sample and included in Table 7.1. One of the key assumptions in the development of the model was that the projected bead width in a multi-pass overlay is the same as the single-bead width. Consequently, the projected bead width in each overlay is also compared to the width of the matching single bead.

Sample	Height (mm)	Overlap	IP Temp. (^{o}C)	Penetration (mm)		Ripple (mm)		Width (mm)	
				Predicted	Measured	Predicted	Measured	Single Bead	Projected Width
A	2.0	0.48	25	1.8	2.0	0.3	0.5	11.6	10.0
B	3.0	0.44	25	1.7	1.5	0.5	0.5	10.8	10.5
C	4.3	0.50	25	2.0	1.8	0.5	0.3	15.9	15.5
D	4.1	0.55	400	2.3	2.1	0.4	0.2	17.9	16.5
E	4.3	0.65	25	0.9	0.9	0.2	0.1	11.4	11.5
F	4.3	0.69	400	1.3	1.3	0.1	0.2	12.8	13.0
G	5.2	0.62	25	1.3	1.3	0.3	0.2	13.2	12.5
H	6.1	0.52	25	2.0	1.7	0.6	0.2	16.8	16.0

Table 7.1: - A comparison of the geometric models predictions with experimental results.

It can be seen that there is good agreement between the penetrations predicted by the geometric model and the experimental results. The agreement is acceptable over the

entire range of welding conditions that were considered, and it is similar to that achieved by the k-ε model with an empirical correction. There is also reasonable agreement between the predicted ripples and those measured in experiment for all conditions except "H". Furthermore, for each of the eight overlays, the projected bead width remained virtually unchanged from the width of the matching single-bead deposit.

There appears to be a tendency to overestimate the average penetration for the overlays deposited at low speeds (*i.e.* conditions "C", "D" and "H"). For the overlays deposited at higher travel speeds, (*i.e.* "A", "B", "E", "F" and "G") this trend does not appear to exist. It is most likely that, at slow welding speeds, the discrepancy is caused by the weld pool flowing under the influence of gravity. Under these conditions the weld pool is larger, the cooling times are slower, and the weld pool has more time to flow. Flow occurs both in front of the electrode and behind it. The flow in front of the electrode may result in material from the previous bead flowing on to molten substrate, thus reducing the amount of substrate that is melted and exposing more of the previous bead to the arc. Flow behind the electrode causes the bead profile to deviate from a parabolic shape and form a flatter, wider bead. Consequently, when the next bead is deposited, the arc is forced to melt more of the previous bead and less of the substrate.

The peak-to-valley ripple is a feature that is difficult to predict accurately because the surface of an overlay is not perfectly smooth. The predictions of the model do, however, appear to be reasonable, particularly for those samples deposited at moderate-to-high speeds. There is a tendency, at slow travel speeds, (*i.e.* for "C", "D" and "H") to overestimate the ripple. Once again, this can be explained in terms of weld bead

flattening caused by gravity-induced flow. This flattening effect is particularly prevalent in high overlays such as "H".

It would appear that the major sources of error for this model are related to the geometry of the overlay and not the thermal or physical properties. For both the penetration and peak-to-valley ripple, the most noticeable discrepancies occur when the assumption of a parabolic bead profile is least accurate. If the differences in thermal properties between the overlay material and substrate were the principal causes of error, one might expect, for example, the penetrations to be consistently overestimated. High-chromium white irons have a lower melting point than steels, typically 1220-1250^{o}C, compared with 1450-1500^{o}C. Consequently they are likely to be the first material to melt and they may melt preferentially to steel, thus reducing the penetration of the overlay. However, such a consistent discrepancy is not observed in the experimental data.

The apparent insensitivity of the overlay penetrations to thermal or physical property differences is an interesting point. During the course of the experiments it was observed that, if the same amount of heat were to be delivered to each material, white iron would melt in greater quantities than steel. This observation, however, does not necessarily create a problem for the model. It was noted in section 6.3 that, to define the steady-state dilution, it is necessary to know only the quantity of material that is deposited per pass and the amount of new substrate that is melted per pass. The quantity of the previous bead that is melted will not matter provided that it does not influence the amount of new substrate that is melted.

7.6 GAS-TUNGSTEN ARC WELDING EXPERIMENTS

A series of experiments were planned to further investigate the influence of thermal properties on the location of the fusion line. In these experiments the intention was to maintain a gas-tungsten arc while travelling along the interface between two flat bars, one being a steel and the other a white-iron casting. The flat surface prior to welding would eliminate the effects of overlay geometry, and the partitioning of melting between the two materials could then be identified. A schematic representation of the experiment is given in Figure 7.8.

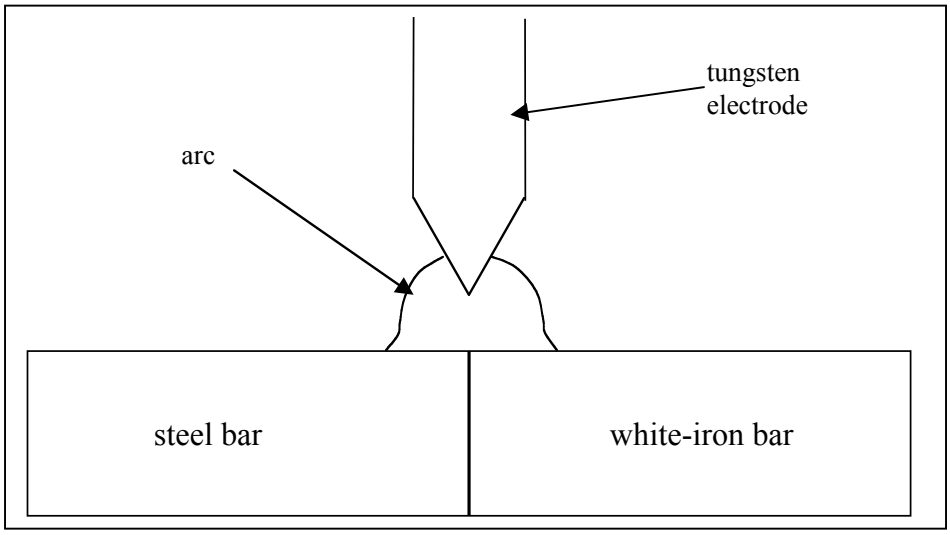

Figure 7.8: - Schematic representation of the GTAW welding experiments.

GTAW welding was selected for two reasons. The problem is simplified by removing the influence of metal transfer. In addition, GTAW welding removes the possibility of the electrode wandering and thus influencing the partitioning of heating between the two materials. (FCAW welding consumables usually acquire some degree of curvature when they are wound on to a reel. When welding commences, this curvature may cause the

length of electrode that is protruding from the contact tip to "wander" from the desired position.)

7.6.1 Description of Experiments

There were four welds in total. In each case the weld configuration was a partial-penetration square-butt weld approximately 300mm in length. All welds were autogenous and the materials to be welded were flat bars 50mm wide, 350mm long and 25mm thick. In all cases both bars were tack welded on to a flat base plate prior to the experiment as shown in Figure 7.9.

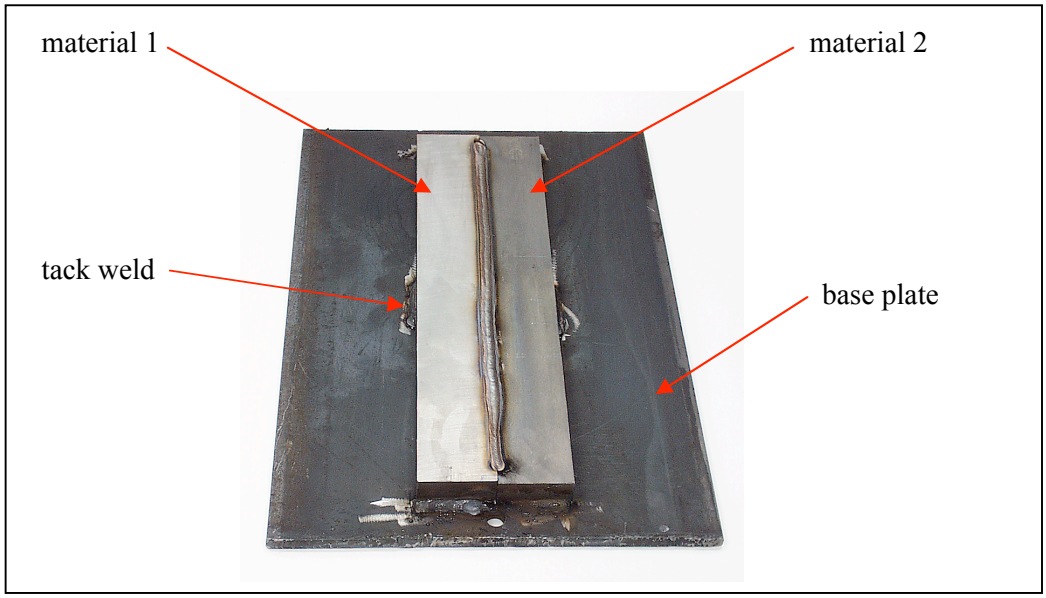

Figure 7.9: - The configuration of a sample in the GTAW welding experiments.

Two holes were drilled in each base plate for work-return leads; one at each end and both on the centre line of the weld, so that the probability of arc blow was reduced. The tack welds, which provided the electrical contact between the work and the base plate, were also distributed symmetrically about the weld centre line. Great care was taken to ensure that the tungsten electrode was aligned with the interface between the materials to

be welded. The electrode was moved down towards the seam, so that it almost touched the bars, and was aligned at both ends before being retracted to the desired arc length.

The experimental plan is summarised in Table 7.2. In one of the experiments a white-iron casting is welded to a steel bar, a steel-to-steel weld is included and a white-iron bar is also welded to another white-iron bar. Finally, a steel bar is welded to a white-iron bar with a 2mm step at the interface. In this case the white-iron bar was closest to the welding electrode. All of the steel bars used in the experiments were cold-finished carbon steels, containing 0.2 wt.% C. The white-iron bars were sand castings containing 19.6% Cr, 3.95% C, 1.5% Mo, 0.9% Mn and 0.9% Si by weight. This composition was chosen as it is representative of that which might be achieved in a low-dilution 4mm high weld overlay.

Experiment No.	Material 1	Material 2	Step (mm)	Arc Length (mm)	Voltage (V)	Current (A)	Speed (mm/min)
I	steel	steel	0	2.5	14.3	350	400
II	white iron	white iron	0	2.5	14.4	350	400
III	steel	white iron	0	2.5	13.6	350	400
IV	steel	white iron	2	1.0 (from near surface)	11.6	350	400

Table 7.2: - A summary of the welding conditions for each of the four GTAW experiments. Voltages and currents were recorded on the CSIRO welding monitor described in section 3.2.

In all cases the direct-current, electrode-negative (DCEN) configuration was selected to prevent melting of the 4mm diameter, ceriated tungsten electrode. The electrode was ground so that it had a conical tip with an included angle of 90^{o}. A large angle was selected to reduce the current density (Hiraoka *et al.*, 1986), and therefore produce a weld bead that was wide, with a penetration profile that was approximately parabolic in shape. A helium-rich shielding gas was selected as this also favours the formation of wide beads (AWS Welding Handbook, 1991). The shielding gas comprised 75 vol.% helium with the balance being argon. A summary of other parameters is included in Table 7.2.

7.6.2 Results

After the experiments were completed, each weld was sectioned, polished, etched and photographed. For the steel-to-steel weld the etchant was 2% Nital, for the steel-to-white-iron samples 2% Nital was used followed by Vilella's reagent, whereas the white-iron-to-white-iron weld was etched with Vilella's reagent only. The photographs are shown in Figures 7.10. For each experiment, the cross-sectional area of material that was melted from each of the bars was measured and included in Tables 7.3. The melted areas were measured by printing the images, reconstructing the original surfaces of the bars, cutting the melted sections from the images and then weighing them. It can be seen that there are two results listed for experiment I. For the steel-to-steel sample the weld pool solidified, in some instances, before it was able to flow and weld the bars together. This sample was sectioned twice, once where the weld pool was intact and once where it was not, and results are shown for both cases.

Similar Materials

Experiment	Material	Area Melted (left-hand side), mm^2	Area Melted (right-hand side), mm^2	Total Area Melted, mm^2
I	steel (unbroken weld)	6.6	7.9	14.5
I	steel (broken weld)	10.9	7.7	18.6
II	white iron	13.0	14.3	27.3

Dissimilar Materials

Experiment	Steel Melted, mm^2	White-Iron Melted, mm^2	Total Area Melted, mm^2
III	11.2	7.7	18.9
IV	5.5	10.6	16.1

Tables 7.3: - A summary of the results of cross-sectional area measurements for the GTAW welding experiments.

7.6.3 Discussion

Figures 7.10 and, in particular, the welds between similar materials show that the alignment of the tungsten electrode was accurate. These welds were distributed evenly across the interface between the bars. While the areas measured for the broken steel-to-steel weld indicate that, at that particular location, melting occurred preferentially on one side of the interface, a close examination of the image reveals that the edges of the weld pool were approximately equi-distant from the interface. Thus, the apparent bias may have been related to the location of the weld pool at the moment the arc passed by.

It is evident from experiments I and II that, for a given set of welding parameters, more material will melt when the substrate is a high-chromium white iron than when it is mild steel. This result is not unexpected since high-chromium white irons have a lower melting point than steels. It is also evident from experiment I that the location of the weld pool affects the amount of material that is melted, with 25 – 30% more material being melted when the weld pool was broken than when it was continuous. This result indicates that the weld pool does, to some extent, cushion the surrounding material from further melting, as was suggested in an early work by Farmer (1966b).

Experiment III provided an unexpected result in that more steel was melted than white iron. One might have expected a greater quantity of white-iron to melt given its lower melting point. It would appear, therefore, that heat from the arc was delivered preferentially to the steel. Such a bias may have been introduced by asymmetric convection within the weld pool. Lancaster (1986) illustrated how, when welding dissimilar materials, asymmetric surface tension gradients may result in the preferential melting of one material (see Figure 7.11). The superheated molten metal immediately

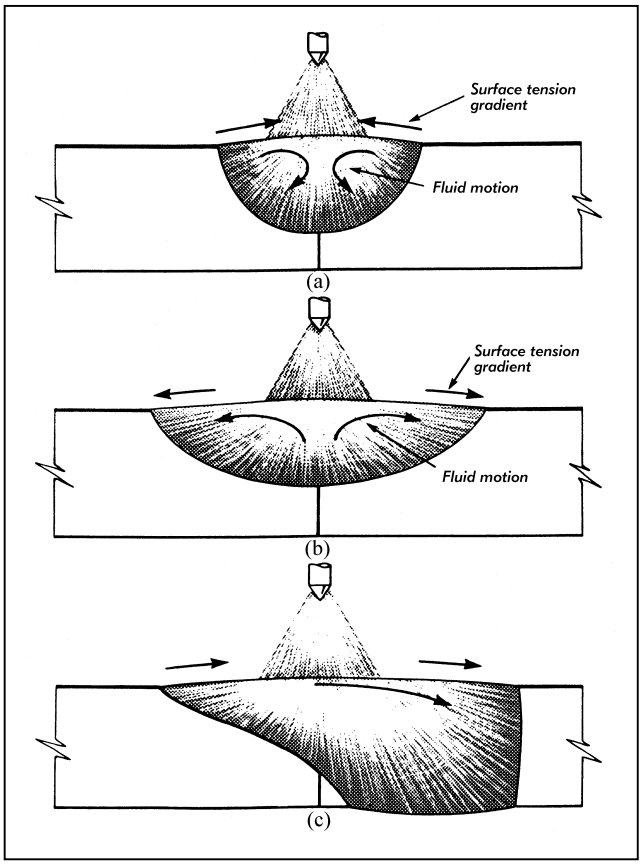

Figure 7.11: - The effects of surface-active elements on weld pool convection and fusion zone geometry in GTAW weldments (after Lancaster, 1986): (a) surface-active elements present; (b) surface-active elements absent; (c) dissimilar materials.

under the arc will be transported toward the material with the higher surface tension, resulting in the preferential melting of that material. The results of experiment I also support this argument. The fact that the weld pool was frequently broken in the steel-to-steel weld suggests that the surface tension of the liquid steel was high enough to prevent the pool from recombining. Furthermore, the weld pool remained intact for all welds with white iron, which suggests that the liquid white iron had a lower surface tension than the liquid steel. It should be noted, however, that the effects of asymmetric convection were not observed in overlays A to H, which were deposited by open-arc

FCAW. This suggests that the molten globules being transferred to the weld pool play an important role in disturbing such convection patterns. It is possible that, in this way, the globules promote a relatively uniform distribution of heat throughout the pool.

The role played by the molten globules in determining the distribution of heat may explain why the geometric model can accurately predict average overlay penetrations. The geometric model superimposes a melting parabola, defined by the single-bead dilution, on to the profile of the previous bead to predict the fusion line. The implicit assumptions are that the heat is distributed uniformly, and that the material properties are the same for both materials. The fact that the material properties for the white iron are different to those of the steel, however, may not significantly affect the amount of steel that is melted. If the heat is distributed uniformly and, to a first-order approximation, the amount of steel that is melted remains unchanged, then the predicted overlay penetration will be accurate.

If heat were to be distributed uniformly throughout the weld pool, one might expect that the cross-sectional area of material that is melted in an overlapping bead, A_m, will be given by the following equation:

$$A_m = \gamma A_{st} + (1 - \gamma) A_{wi} \quad \text{..... (7.9)}$$

where A_{st} and A_{wi} are the areas of substrate that would be melted in matching single beads deposited on steel and white-iron substrates respectively, and γ is an energy partitioning coefficient. A_m excludes the area that is contributed by deposited material. Equation 7.9 is an energy balance, and it suggests that any energy that is not used in the melting of steel must be available for the melting of white iron and vice versa. This

definition for α is consistent with the definition given in section 6.8. The validity of equation 7.9 is tested in Tables 7.4 and 7.5.

Steel Melted in Experiment I	14.5 mm^2
Steel Melted in Experiment III	11.2 mm^2
Estimate for α	0.77
Total White Iron Melted in Experiment II	27.3 mm^2
Predicted White Iron Melted in Experiment III	***6.2 mm^2***
Actual White Iron Melted in Experiment III	***7.7 mm^2***

Table 7.4: - The procedure for predicting the area of white iron that was melted in Experiment III using equation 7.9.

White Iron Melted in Experiment II	27.3 mm^2
White Iron Melted in Experiment III	7.7 mm^2
Estimate for (1 - α)	0.28
Total Steel Melted in Experiment I	14.5 mm^2
Predicted Steel Melted in Experiment III	***10.4 mm^2***
Actual Steel Melted in Experiment III	***11.2 mm^2***

Table 7.5: - The procedure for predicting the area of steel that was melted in Experiment III using equation 7.9.

The results in Tables 7.4 and 7.5 indicate that, in this instance, the predictions made by equation 7.9 appear to be reasonable. The largest error was observed in Table 7.4 where the quantity of white iron that was melted was underestimated by approximately 20%. More work, however, will be required to confirm the results presented in this section and, in particular, the validity of equation 7.9.

Finally, another cause of preferential melting was demonstrated in experiment IV. If the arc gap between the electrode and one of the materials is reduced, then the heating will be biased toward that material. The results of experiment IV were not used to test the validity of equation 7.9 as a different arc length (and hence heat input) was used to that in the other experiments.

7.7 LIMITATIONS OF THE MODEL

The geometric model accurately predicts the steady-state penetration of a multi-pass overlay under many different welding conditions. There are, however, some situations in which the accuracy of the model may be compromised. This section describes some of the limitations of the geometric model.

7.7.1 Sensitivity to Input Data

The predictions of the model are sensitive to the input data. If, for example, the correct single-bead dilution is entered but the bead width is overestimated by 2mm, say, an error in penetration of up to 0.5mm may result in some circumstances. Errors in predictions of bead width or single-bead dilution change the depth-to-width ratio of the melting parabola and hence the predicted penetration. In practice the best predictions for multi-pass overlays are achieved by depositing a single bead with the chosen welding parameters, and measuring the single-bead width and dilution. If the overlay welding conditions deviate significantly from the conditions that were used for the single-bead deposit, accurate predictions may still be achieved by normalising the single-bead data with the procedure outlined in section 6.6.

7.7.2 Transient Conditions

The geometric model predicts the overlay dilution and geometry under steady-state conditions. It cannot predict the dilution for the transient period at the commencement of deposition, nor can it predict the number of beads that will be required before a steady-state condition is reached.

7.7.3 Inter-Pass Temperature

The predictions of the model are only accurate if the inter-pass temperature is maintained at the same value that was assumed (or used) to obtain values for the single-bead dilution and width. When depositing a multi-pass overlay the inter-pass temperature can deviate significantly from its initial value due to cumulative heating of the substrate. For the model to be accurate, and to keep the penetration to a minimum, appropriate cooling measures or time delays need to be introduced.

Care also needs to be taken when depositing overlays bi-directionally. If deposition proceeds without an appropriate delay at each end, the previous bead will still be very hot. Under these circumstances an alternating high-low penetration profile is observed, such as the one shown in Figure 7.12. This sample was deposited specifically to demonstrate this phenomenon. Such a penetration profile may result in the preferential wear of every second bead in the overlay, and reduce the wear life of the component.

The substrate in Figure 7.12 was a 0.2 wt.% C steel bar 350mm long, 100mm wide by 10mm thick. The welding consumable was equivalent to consumable B (see section 3.2). Four pairs of beads were deposited with each bead being approximately 300mm in length. The first bead was deposited and the arc was maintained while the welding head

stepped over and immediately deposited the second bead. The plate was then left to cool for several minutes before the procedure was repeated. The intention was to reproduce the conditions that might arise, for example, at the end of a large pipe that is being surfaced bi-directionally. For all of the beads, the nominal welding parameters were 28V; 400A; 20mm work distance; 800mm/min travel speed; and 6mm step-over. The section shown in Figure 7.12 was taken approximately 40mm from the position where the welding head turned around for the second pass.

7.7.4 Bead Profile

Under certain welding conditions the profile of the fusion line may deviate from a parabolic shape. Kim and Na (1995), for example, showed that a finger-like penetration profile is favoured when a low work distance is used (see section 2.3). The predictions of the model may be less accurate if the penetration profiles of individual beads differ significantly from a parabolic shape.

In other instances a welding consumable may appear to be susceptible to random variations in penetration. Some examples were observed in the current work and one is shown in Figures 7.13. These figures show two sections through the same single-bead deposit that were separated by only 10mm of travel. Such random and sudden changes in penetration may be related to the molten globules detaching from the consumable electrode at irregular intervals. For example, a temporary reduction in the detachment frequency would initially result in a smaller weld pool. More of the underlying substrate would then be exposed to the heat of the arc and a temporary increase in the penetration would result. If the penetration profile is inconsistent, it is important to obtain more than

one measurement of the single-bead dilution and enter an average value into the geometric model.

7.8 CONCLUSIONS

A geometric model has been developed that accurately predicts the steady-state dilution of high-chromium white iron multi-pass overlays. The model is based on the assumption that both the steady-state bead profile and the fusion line can be represented by parabolic functions. The predictions of the model are most accurate when the welding conditions include a high travel speed as, under these circumstances, the bead profile closely resembles a parabola. The accuracy is acceptable, however, at lower travel speeds. The most significant limitation associated with the model is its sensitivity to the input data. Nevertheless, the model has been shown to work for two high-chromium, high-carbon type consumables, and it is anticipated that it will generally apply to similar consumables.